



1 Relaxed Eddy Accumulation based Flux measurement of Atmospheric Inorganic Acidic Species over

2 Cropland under the Long-Term Exposure to Chemical Industry Emissions in a Chinese Megacity

3

4 Jingya Hua, Xinyu Wang, Yulian Wei, Jieya Sun, Zongjun Li, Zhongliang Huang, Qiongqiong Wang,

5 Huan Yu\*

6

7 *Department of Atmospheric Science, School of Environmental Studies, China University of Geosciences,*

8 *Wuhan 430074, China*

9 \*corresponding author, yuhuan@cug.edu.cn

## 10 Abstract

11 China hosts a large number of industrial parks in densely populated areas, where pollutant emissions

12 turn surrounding lands into high-deposition-load hotspots. Long-term exposure may alter

13 physicochemical properties of soils and vegetation, leading to complex sink-source transitions of

14 land surface. The lack of local flux data impedes integrated air-soil-water pollution control. We

15 developed a Relaxed Eddy Accumulation system capable of simultaneous flux measurements of

16 eight inorganic species (HNO<sub>3</sub>, HONO, SO<sub>2</sub>, HCl, nitrate, nitrite, sulfate, chloride). System

17 characterization showed detection limits of  $6.1 \times 10^{-4}$ – $2.4 \times 10^{-1}$   $\mu\text{g m}^{-2} \text{s}^{-1}$  and flux precisions of

18 3.0%–29.5% with main uncertainty contributions from mass analysis and lag time inaccuracy. Flux

19 measurement conducted at a vegetable cropland adjacent to chemical industry facilities revealed

20 that HONO and nitrate fluxes at this site were 1–2 orders of magnitude higher than those reports in

21 the literature. Bidirectional fluxes of the species indicate the cropland acts as both source and sink;

22 but winter average showed net emission fluxes only for HONO and nitrite (mean daily 53.0 and

23  $11.5 \mu\text{mol m}^{-2} \text{d}^{-1}$ ). Gross upward emission fluxes of HNO<sub>3</sub> and HONO were  $1.1 \pm 0.9 \mu\text{g m}^{-2} \text{s}^{-1}$

24 and  $0.4 \pm 0.4 \mu\text{g m}^{-2} \text{s}^{-1}$ , respectively, during the winter observation period. HNO<sub>3</sub> gross emissions

25 were enhanced by elevated turbulence, while HONO emissions were promoted at lower ambient



26 temperatures. This study provides observational constraints for acidic species flux parameterization  
27 over industrial-impacted croplands and informs air pollution control and agro-ecological protection  
28 strategies.

29

30 **Keywords** Atmospheric Inorganic Acidic Species; air-surface flux; Relaxed Eddy Accumulation;  
31 measurement uncertainty and detection limit; cropland; Long-Term Influence of Chemical Industrial  
32 Emissions

33

#### 34 **1. Introduction**

35 Atmospheric inorganic acidic species mainly include gaseous sulfur dioxide (SO<sub>2</sub>), nitric acid  
36 (HNO<sub>3</sub>), nitrous acid (HONO), and hydrogen chloride (HCl), as well as their particulate-phase  
37 counterparts: sulfate (SO<sub>4</sub><sup>2-</sup>), nitrate (NO<sub>3</sub><sup>-</sup>), nitrite (NO<sub>2</sub><sup>-</sup>), and chloride (Cl<sup>-</sup>). Dry deposition is a key  
38 removal pathway for these acidic pollutants, reducing their ambient concentrations and attenuating  
39 regional transport. Atmospheric dry deposition of sulfur and nitrogen species provides a pivotal nutrient  
40 supply for crop growth and ecosystems (Galloway 1995, Poor et al. 2001, Shen et al. 2018, Vitousek and  
41 Howarth 1991). However, high deposition flux induces physiological stress in crops (Aber et al. 1998),  
42 disrupts their normal metabolism, photosynthesis and respiration. Furthermore, the deposition of acidic  
43 species may exacerbate soil acidification and trigger eutrophication of surface water and groundwater  
44 (van Breemen and van Dijk 1988).

45 Most existing measurements on dry deposition fluxes of atmospheric inorganic acidic species were  
46 conducted in forest (Farmer et al. 2013, Farmer et al. 2011, Gordon et al. 2011, Hansen et al. 2015,  
47 Meyers et al. 1989, Nguyen et al. 2015, Pryor et al. 2002, Pryor et al. 2001, Ren et al. 2011, Sievering et



48 al. 2001, Xu et al. 2021, Zhang et al. 2012, Zhou et al. 2011), grassland (Huebert et al. 1988, Huebert  
49 and Robert 1985, Myles et al. 2007, Nemitz et al. 2009, Nemitz et al. 2004, Rattray and Sievering 2001,  
50 Rumsey and Walker 2016, von der Heyden et al. 2022), and agricultural ecosystems (Laufs et al. 2017,  
51 Meng et al. 2022, Meyers et al. 1998, Meyers et al. 2006, Shaw et al. 1998). Wuhan, a megacity in central  
52 China, hosts a large number of iron, steel and petrochemical industry facilities in its urban and suburban  
53 areas, which are closely interspersed with extensive farmland. Industrial processes discharge large  
54 amounts of pollutants, rendering adjacent farmlands high-deposition-load zones of acidic species. In  
55 addition to potential adverse human health risks from dietary and respiratory exposures, long-term  
56 exposure to industrial emissions may alter the physicochemical properties of vegetation and soil, making  
57 deposition pathways and resistances of atmospheric acidic species differ from those over natural  
58 farmlands. With long-term exposure to industrial emissions, farmlands may shift from sinks to potential  
59 emission sources of acidic species, e.g., fugitive dust from farmlands and widely known HONO release  
60 from soil (Su et al. 2011). The co-occurrence of deposition, surface emissions and possible near-ground  
61 chemical reactions complicates the sink and source dynamics of acidic species in farmlands and brings  
62 large uncertainties to the development of deposition resistance parameterizations for this type of  
63 ecosystem. To date, no quantitative measurement on acidic species fluxes has been conducted in this  
64 specific habitat. The lack of relevant flux data constrains the development of effective air pollution  
65 control strategies and agro-ecological protection practices in such regions.

66 Eddy covariance (EC) (Farmer et al. 2013, Nguyen et al. 2015), relaxed eddy accumulation (REA)  
67 (Hansen et al. 2015, Matsuda et al. 2015, von der Heyden et al. 2022, Xu et al. 2021), gradient  
68 measurement (Nemitz et al. 2009, Rumsey and Walker 2016), and flux chamber methods (Scharko et al.  
69 2015) are widely used for atmospheric inorganic acidic species flux determination. The REA is a



70 conditional sampling technique to measure trace atmospheric components for which fast response  
71 sensors (>10 Hz) required for EC are not available. The REA has notable advantages for field applications:  
72 simultaneous multi-species flux measurements and lower cost than the EC method. In this study, we  
73 developed an REA system and conducted a flux measurement campaign in a cropland immediately  
74 adjacent to an urban chemical industrial park in winter, the typical haze season of Wuhan. The main  
75 objectives of this study were: (1) to characterize the flux measurement uncertainty and detection limit  
76 and precision of the REA system; (2) to determine the flux of atmospheric acidic species over the  
77 farmland ecosystem under the long-term influence of chemical industry emissions; (3) to estimate the  
78 gross emission fluxes of HONO and HNO<sub>3</sub> from the farmland based on mass conservation and dry  
79 deposition resistance model.

## 80 **2. Experimental section**

### 81 **2.1 Relaxed eddy accumulation technique**

82 First proposed by Businger and Oncley (1990), the REA method measures the vertical flux of  
83 atmospheric species by separating air into updraft and downdraft sampling reservoirs based on high-  
84 frequency vertical wind velocity measurements. Flux is derived from the difference of average  
85 concentrations between the two reservoirs and the bulk weighting of two turbulence statistics that can be  
86 stably measured over a sampling interval:

$$87 \quad F = \sigma_w \beta (C_{up} - C_{down}) \quad (1)$$

88 where  $C_{up}$  and  $C_{down}$  are the average concentrations in updraft and downdraft,  $\sigma_w$  is the standard deviation  
89 of vertical wind speed ( $w$ ) and  $\beta$  is a dimensionless proportionality coefficient universal for scalars,  
90 which can be calculated from sonic anemometer measurements of sensible heat flux  $\beta = \frac{W'T'}{\sigma_w(T_{up}-T_{down})}$ .

91 This framework enables stable and controllable flux calculations, with results highly consistent with EC



92 measurements(Gaman et al. 2004, Karl et al. 2005, Lee et al. 2005, Pryor et al. 2007).

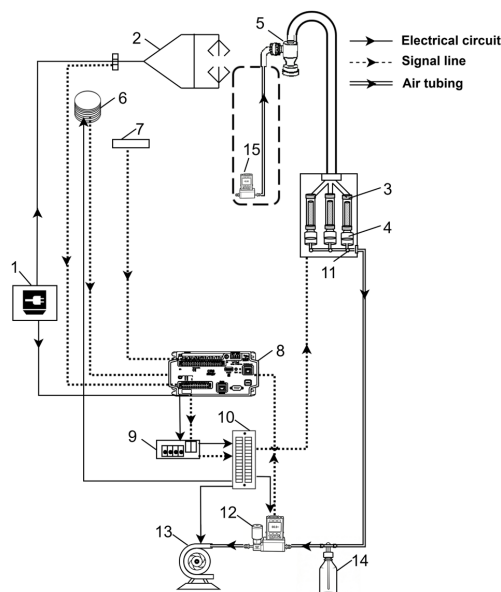
93 We built an REA sampling system for simultaneous sampling of gaseous and particulate inorganic  
94 acidic species (**Figure 1**). High-frequency (10 Hz)  $w$  was measured by a 3D sonic anemometer (CSAT3B,  
95 Campbell Scientific Inc., Logan, Utah, USA). Each of three sampling channels (updraft, downdraft,  
96 dead-band) was equipped with an annular denuder (URG-2000-30×242-3CSS, URG, Chapel Hill, North  
97 Carolina, USA) for gaseous HNO<sub>3</sub>, HONO, SO<sub>2</sub> and HCl collection and a filter cartridge with a 2 μm  
98 PTFE filter (Whatman 7592-104, 46.2 mm, PP ring-supported) installed downstream for particulate NO<sub>3</sub>,  
99 NO<sub>2</sub>, SO<sub>4</sub><sup>2-</sup>, and Cl<sup>-</sup> collection. The three sampling channels shared a single PM<sub>2.5</sub> cyclone inlet (URG-  
100 2000-30EH, URG, Chapel Hill, North Carolina, USA), a 1.35-meter stainless steel inlet tube and a  
101 sampling pump (KNF N026.1ANE, KNF Neuberger GmbH, Freiburg, Germany). Notably, the system  
102 features expandable sorbent tube channels for simultaneous VOC flux measurements, but only its  
103 performance for inorganic acidic species is reported herein. The sampling flow rate was set to a nominal  
104 10 standard liters per minute with a mass flow controller (MFC, No. 12 in **Figure 1**) mounted on the inlet  
105 side of the pump. The flow in the inlet tube was in the laminar regime (the Reynolds number ~1200),  
106 which is essential for the denuders to work properly (i.e., efficient gas-particle separation). The lag time  
107 for air to travel from the inlet to the sampling filter membrane was calculated according to total internal  
108 volume of air tubing and volumetric flow rate at the onset of each sampling run. For example, it was 3.1  
109 s at ambient temperature 15 °C.

110 A CR1000X data logger (Campbell Scientific Inc., Logan, Utah, USA) served as the system central  
111 controller, responsible for data acquisition, storage, and conditional sampling logic execution.  
112 Conditional switching between the sampling channels was checked at 2 Hz to balance high-frequency  
113 flux loss and perturbations to the laminar flow in the denuders. Three-minute running mean ( $\bar{w}$ ) and



114 standard deviation ( $\sigma_w$ ) of  $w$  were calculated in real time to trigger the actuation of three solenoid valves  
115 (Numatics LS02M6F00B, Emerson Electric Co., St. Louis, Missouri, USA): updraft sampling at  $w > \bar{w}$   
116  $+ 0.6\sigma_w$ , downdraft sampling at  $w < \bar{w} - 0.6\sigma_w$ , and dead-band airflow within the  $w \pm 0.6\sigma_w$  range. Lag time  
117 was taken into account to determine the precise timing of solenoid valve switching. The CSAT3B sonic  
118 anemometer had a minimum response time of 0.7 ms, with effectively zero signal latency to the data  
119 logger. The total end-to-end system time delay was 17.9 ms, including 10–15 ms for solenoid valve  
120 response, 1.4 ms for relay actuation, and 4 ms for real-time calculation and command execution. This  
121 short delay time minimized temporal misalignment between wind measurements and the sampling,  
122 reducing updraft/downdraft mixing and flux result distortion.

123 The REA device was mounted on a 4-meter-high flux tower. The sonic anemometer was installed  
124 at the tower top, oriented due north (the prevailing local winter wind direction). The inlet of the PM<sub>2.5</sub>  
125 cyclone was vertically aligned with the anemometer, with a horizontal separation of 0.3 m. The sampling  
126 enclosure housing the sampling unit and solenoid valves was fixed on the tower 0.7 m below the  
127 anemometer to minimize airflow disturbance around the anemometer. A Vaisala Weather Transmitter  
128 WXT536 was also installed near the top of tower to provide supporting measurements of air pressure,  
129 air temperature, relative humidity, precipitation, wind speed, and wind direction. The pump and other  
130 REA components were mounted at the tower base.



131

132 **Figure 1.** Schematic diagram of the REA flux sampling device for atmospheric inorganic gas and  
133 particles. 1. Power supply; 2. 3D sonic anemometer; 3. Denuder tube; 4. Filter-pack cartridge; 5. Cyclone  
134 inlet; 6. Vaisala Weather Transmitter; 7. Thermocouple; 8. Data logger; 9. Relay; 10. Terminal block for  
135 signal and power distribution; 11. Fast switching valves; 12. Mass flow controller (MFC); 13. Pump; 14.  
136 500ml buffer bottle; 15. Mass flow meter (MFM) used in test runs only.

## 137 2.2 Sample collection and chemical analysis

138 The Wuhan Chemical Industrial Park (WCIP) is located northeast to the urban area of Wuhan. The  
139 WCIP covers 71.64 km<sup>2</sup> and hosts petrochemical, fine chemical, and building material industries. The  
140 flux tower was installed in the center of a vegetable-growing cropland within the 7.3 km<sup>2</sup> Beihu Farm,  
141 which is immediately adjacent to the WCIP. The nearest petrochemical facility is ~1.0 km to the north of  
142 the tower (**Figure S1**). The tower is situated on flat terrain with no obstructing buildings or trees within  
143 a 500 m radius of the tower, ensuring undisturbed airflow measurements. Field sampling was performed  
144 from 29 October to 30 December 2025, with 11 valid sampling days in cloudy or sunny rain-free weather.



145 Each sampling day included three 4-hour sampling periods (morning: 8:00–12:00; afternoon: 12:30–  
146 16:30; evening: 17:00–21:00). Flux footprints were calculated using the FFP online tool developed by  
147 (Kljun et al. 2015). Input wind and site information for the model included sampling time, measurement  
148 height, zero-plane displacement, wind speed, wind direction, Obukhov length, and friction velocity. The  
149 cumulative flux footprint over the entire sampling campaign is presented in Supplementary **Figure S1**.

150 One set of denuders and filter samples, plus field blanks, was collected per one sampling period.  
151 The annular denuders were freshly coated with a sorbent layer for inorganic acidic gases collection prior  
152 to sampling, in accordance with the U.S. EPA standard protocol (Fitz and Millar, 2002). The coating  
153 solution 1% (w/v) sodium carbonate in water and 1% (v/v) glycerol in a methanol-water mixture (1:1,  
154 v/v) was prepared fresh immediately before use. For coating, 10 mL of the solution was injected into the  
155 denuder, which was then sealed at both ends, inverted and rotated repeatedly to ensure uniform inner-  
156 wall coating, and purged with 99.999% high-purity nitrogen until complete methanol and water  
157 evaporation. Theoretically, the sodium carbonate sorbent layer has an absorption capacity of 6 mg SO<sub>2</sub>,  
158 even assuming that only 10% of the sodium carbonate solution was effectively coated onto the inner wall  
159 of the annular denuder. The total sampling volume per denuder channel was 0.6 m<sup>3</sup>, which would contain  
160 a maximum of only 5 µg SO<sub>2</sub> based on the highest ambient SO<sub>2</sub> concentration documented in local air  
161 monitoring records. Even when accounting for coexisting acidic gaseous species, the 0.6 m<sup>3</sup> sampling  
162 volume is still well below the breakthrough volume of the denuder. Coated denuders were sealed with  
163 PTFE caps until use.

164 After each 4-hour sampling run, annular denuders and filters were disassembled for subsequent  
165 offline chemical composition analysis. The inorganic salts formed by absorbed acidic gases in the  
166 denuder sorbent layer were eluted with 10 mL of 0.05% (v/v) H<sub>2</sub>O<sub>2</sub> aqueous solution, which oxidizes



167 sulfite ( $\text{SO}_3^{2-}$ , the product of  $\text{SO}_2$  absorption) to the more stable  $\text{SO}_4^{2-}$ . Particulate-phase inorganic ions  
168 collected on the filters were ultrasonically extracted into 10 mL of ultrapure deionized water. Then, the  
169 inorganic ions were analyzed with ion chromatography (Dionex, ICS-1100, Thermo Scientific,  
170 Massachusetts, USA). Before running analysis, the system was calibrated using standard solutions.  
171 Inorganic ions in a sample solution were identified by comparing with the chromatographic peaks of the  
172 known standards and quantified using calibration curves after field blank subtraction.

### 173 3. Results and discussion

#### 174 3.1 Uncertainties and detection limit of flux measurement

175 High-frequency flux losses may occur from two sources: (1) valve switching frequency below 10  
176 Hz, and (2) laminar flow in the inlet tubing. These two effects combine to cause non-negligible mixing  
177 between consecutive air samples. However, the  $\beta$  coefficient was explicitly determined using temperature  
178 measurements from the sonic anemometer, calculated as  $\frac{W'T'}{\sigma_w(T_{up}-T_{down})}$ , where  $T_{up}$  and  $T_{down}$  were derived  
179 from temperatures sampled under the same switching frequency and  $0.6\sigma_w$  dead-band conditions. The  $\beta$   
180 coefficients for each 4-hour sampling period fell within the typical range of 0.47 to 0.62. This empirically  
181 derived  $\beta$  calibration approach provided a correction for high-frequency losses (Skov et al. 2006). The  
182 remaining source of uncertainty in REA flux measurements arises from the potential biases of the  
183 concentration difference of target species between updraft and downdraft samples ( $C_{up} - C_{down}$ ), the  
184 core term in Equation (1). Concentrations are calculated as  $C_{up} = \frac{M_{up}}{V_{up}}$  and  $C_{down} = \frac{M_{down}}{V_{down}}$ , where  $M$   
185 and  $V$  denote the collected analyte mass and the total air sample volume, respectively, for each reservoir.  
186 Next, we evaluated the uncertainties associated with  $M$  and  $V$  determination, from which the precisions  
187 and detection limits of flux measurement were derived for each species.

##### 188 3.1.1 Uncertainty in air sample volume

189 The stability of the sampling flow rate is critical for accurate sampling control of the REA system.



190 Rapid solenoid valve switching between updraft and downdraft sampling inevitably caused transient  
 191 flow fluctuations. A buffer bottle (No. 14 in **Figure 1**) was installed to mitigate such fluctuations, and a  
 192 calibrated mass flow meter (MFM) was added temporarily for 6 replicate 60-min tests at the sampling  
 193 inlet to measure actual flow rates through the denuders/filters. Flow rate fluctuations at switching  
 194 frequencies of 10 Hz, 2 Hz, and 1 Hz were evaluated, showing that higher switching frequencies induced  
 195 stronger transient flow disturbances, but all transient flow rate fluctuations recorded by the MFM were  
 196 within  $\pm 3\%$  of the MFC reading (**Figure S2**).

197 To quantify the overall error in MFC-derived sample volumes, we calculated the standard deviation  
 198 (SD) of the relative deviation  $\frac{V_{MFC} - V_{MFM}}{V_{MFM}}$ , where  $V_{MFC}$  is the sample volume calculated from flow rate  
 199 readings recorded by the on-board MFC, while  $V_{MFM}$  is the actual sample volume calculated from actual  
 200 flow rates recorded by the calibrated MFM. This metric corresponds to the relative uncertainty of the  
 201 sample volume, accounting for both the precision of MFC readings and their accuracy relative to actual  
 202 sample volume. Values were 0.32% at 10 Hz, 0.16% at 2 Hz, and 0.08% at 1 Hz (**Table 1**), confirming  
 203 that the buffer bottle effectively reduced the impact of flow fluctuations on sample volume accuracy. The  
 204 2-Hz switching frequency used in our field sampling yields a final sample volume relative uncertainty of  
 205 0.14% (updraft) and 0.17% (downdraft).

206 **Table 1.** Relative uncertainty of air sample volume induced by valve switching flow fluctuations and  
 207 relative uncertainty of collected analyte mass induced by lag time inaccuracy

| Parameter                 | Updraft  | Downdraft |
|---------------------------|--|-----------|
| Valve Switching Frequency | Relative Uncertainty of Sample Volume          |           |
| 10 Hz                     | 0.33%  | 0.31%     |
| 2 Hz                      | 0.14%  | 0.17%     |
| 1 Hz                      | 0.08%  | 0.07%     |
| Lag Time Inaccuracy       | Relative Uncertainty of Collected Analyte Mass |           |



|       |        |        |
|-------|--------|--------|
| 0.1 s | 2.64%  | 2.64%  |
| 0.3 s | 6.67%  | 6.72%  |
| 1.0 s | 16.12% | 18.52% |

### 208 3.1.2 Uncertainty in Collected Analyte Mass Induced by Lag Time Inaccuracy

209 The lag time, a key parameter for REA sampling, was pre-calculated prior to each sampling run at  
210 the onset of the sampling run. Flow rate variations during sampling (e.g., due to ambient temperature  
211 changes) induce a time offset  $\Delta t$  between the pre-set and actual lag time, which results in a mass mismatch  
212  $\Delta M$  of the target analyte between the updraft events and the updraft reservoir (or between the downdraft  
213 events and the downdraft reservoir). The relative deviation  $\Delta M/M$  represents the random error in  
214 collected analyte mass induced by lag time inaccuracy, which propagates directly into final flux results.  
215 The magnitude of  $\Delta M/M$  increases with larger updraft-downdraft concentration difference ( $C_{up} - C_{down}$ ),  
216 longer time offset  $\Delta t$ , and more valve switching cycles during sampling.

217 To quantify the relative deviation  $\Delta M/M$  induced by lag time inaccuracy, a 4-hour time series of  
218  $\text{HNO}_3$  concentration and vertical wind was obtained from simultaneous measurements of an iodide-  
219 adduct chemical ionization mass spectrometer (I-CIMS) and the sonic anemometer at the site. The I-  
220 CIMS recorded  $\text{HNO}_3$  at 10 Hz resolution, while the anemometer was used to classify updraft/downdraft  
221 events at 10 Hz. We uniformly scaled updraft and downdraft  $\text{HNO}_3$  concentrations to match the average  
222 updraft-downdraft concentration differences observed in the 33 sampling runs in the campaign,  
223 generating 33  $\text{HNO}_3$  concentration time series for the simulation. A time offset  $\Delta t$  was then introduced  
224 between reservoir sampling windows and actual vertical flow events (updraft or downdraft) to determine  
225  $\Delta M/M$  for each reservoir. Simulation results of  $\Delta M/M$  at  $\Delta t = 0.1$  s, 0.3 s, and 1.0 s for the 33 runs are  
226 showed in **Table S1**. The SD of  $\Delta M/M$  was calculated to quantify the relative uncertainty of collected  
227 analyte mass induced by lag time inaccuracy and presented in **Table 2**. The maximum ambient  
228 temperature variation recorded in a sample run was 8 °C, corresponding to a maximum  $\Delta t$  of 0.1 s; thus,



229 the relative uncertainty at  $\Delta t = 0.1$  s (2.64% for both updraft and downdraft) were adopted for the final  
230 flux uncertainty estimation. The above simulation was performed using  $\text{HNO}_3$  data only due to the lack  
231 of 10 Hz measurements for other species, and we assumed the lag time-induced relative deviations are  
232 identical for all target acidic species. This assumption is valid because all target species are sampled  
233 through identical tubing and valve systems, so their lag time errors are dominated by the same flow  
234 dynamics.

### 235 3.1.3 Uncertainty in mass analysis

236 The overall uncertainty in mass analysis of gaseous target species ( $\text{HNO}_3$ , HONO,  $\text{SO}_2$ , HCl)  
237 consists of two components: the random error in ion chromatography (IC) analysis and the uncertainty  
238 associated with denuder collection efficiency.

239 For  $\text{SO}_2$ , the uncertainty in mass analysis was determined from six replicate tests using a 2 ppbv  
240  $\text{SO}_2$  calibration gas standard, under sampling conditions identical to those used for ambient sampling  
241 (e.g., sampling flow rate, sampling duration, and denuder coating). All replicate samples were pretreated  
242 and analyzed in a single IC batch, giving a mean recovery of 92% and a relative standard deviation ( $RSD$ ,  
243  $\sigma_M/\bar{M}$ ) of 5.8%. The measured mass of  $\text{SO}_2$  collected by the denuder was corrected using the recovery.  
244 The IC analytical precision (denoted  $RSD_{IC}$ ) was determined to be 4.6% from six replicate injections of  
245 a sulfate standard solution with a concentration matching that of typical ambient sample eluents. The  
246  $RSD_{denuder}$  component arising from variability in denuder collection efficiency was then calculated to be  
247 3.5% via Gaussian error propagation  $RSD^2 = RSD_{IC}^2 + RSD_{denuder}^2$ .

248 Certified standard gases for  $\text{HNO}_3$ , HONO, and HCl were not readily available, so the  $\text{SO}_2$ -derived  
249 mean recovery and  $RSD_{denuder}$  of 3.5% were adopted to these species. The IC analytical precisions  $RSD_{IC}$   
250 for  $\text{HNO}_3$ , HONO, and HCl were determined from six replicate injections of  $\text{NO}_3^-$ ,  $\text{NO}_2^-$ , and Cl<sup>-</sup> standard



251 solutions, yielding values of 2.7%, 3.0%, and 3.2%, respectively. The overall mass analysis precisions  
252 (*RSD*) of HNO<sub>3</sub>, HONO, and HCl were calculated to be 4.4%, 4.6%, and 4.7%, respectively, via Gaussian  
253 error propagation.

254 For the four particulate ionic species (NO<sub>3</sub><sup>-</sup>, NO<sub>2</sub><sup>-</sup>, SO<sub>4</sub><sup>2-</sup>, Cl<sup>-</sup>), the variability in filter collection  
255 efficiency was deemed sufficiently small to be negligible. Therefore, the IC analytical precision *RSD*<sub>IC</sub>  
256 was used to quantify the overall uncertainty of mass analysis. The final precisions (*RSD*) of mass analysis  
257 for all eight gaseous and particulate species are summarized in **Table 2**.

#### 258 3.1.4 Flux measurement precision and detection limit

259 Uncertainties in the derived flux were quantified via the Gaussian error propagation. For both  
260 updraft and downdraft, the relative variance of concentration was calculated as:

$$261 \left(\frac{\sigma_C}{C}\right)^2 = \left(\frac{\sigma_M}{M}\right)^2 + \left(\frac{\sigma_V}{V}\right)^2 \quad (2)$$

262 where  $\sigma_M/M$  is the total relative uncertainty of analyte mass measurements, incorporating contributions  
263 from lag time inaccuracy and mass analysis, and  $\sigma_V/V$  is the relative uncertainty of air sample volume  
264 induced by transient flow fluctuations during valve switching. The variance of the updraft-downdraft  
265 concentration difference was then derived as  $\sigma_{\Delta C}^2 = \sigma_{C_{up}}^2 + \sigma_{C_{down}}^2$  for each measurement. The SD of  
266 flux  $\sigma_F = \sigma_w \beta \cdot \sigma_{\Delta C}$  was calculated for each measurement and presented as error bars of flux values in

#### 267 Figure S3.

268 The Method Detection Limit (MDL) of single-measurement flux was calculated via *t*-test method.  
269 The total effective degree of freedom (*df<sub>eff</sub>*) of the combined uncertainty was calculated using the Welch-  
270 Satterthwaite equation. Combined with the pre-set significance level of  $\alpha=0.05$  (two-tailed test), the  
271 corresponding critical value  $t_{\alpha/2, df_{eff}}$  was obtained from the *t*-distribution table. The minimum  
272 detectable concentration difference was calculated as  $\Delta C_{LOD} = t_{\alpha/2, df_{eff}} \times \sigma_{\Delta C}$ , which was then



273 substituted into Equation (1) to obtain the single-measurement flux detection limit:  $F_{LOD} = \sigma_w \beta \cdot$   
 274  $\Delta C_{LOD}$ . The flux measurement precision ( $RSD, \% = (\sigma_F/|F|) \times 100$ ) was therefore calculated only  
 275 for those measurements with  $F > F_{LOD}$ . The ranges of  $F_{LOD}$  and precisions for the eight species are shown  
 276 in **Table 2**. For a given analyte,  $F_{LOD}$  and precision vary with atmospheric concentration and flux in the  
 277 sampling periods.  
 278 **Table 2** Concentration and flux detection limits, mass analysis precision and flux measurement precision  
 279 of the acidic species.

|                               | Concentration detection<br>limit ( $\mu\text{g m}^{-3}$ ) | Mass analysis<br>precision (RSD, %) | Flux measurement<br>precision (RSD, %) | Flux detection limit<br>( $\mu\text{g m}^{-2} \text{s}^{-1}$ ) |
|-------------------------------|---|-------------------------------------|--|--|
| HNO <sub>3</sub>              | 0.027   | 4.4                                 | 6.1–27.1                               | $1.5 \times 10^{-2}$ – $2.1 \times 10^{-1}$                    |
| HONO                          | 0.034   | 4.6                                 | 4.3–22.6                               | $1.5 \times 10^{-2}$ – $1.2 \times 10^{-1}$                    |
| SO <sub>2</sub>               | 0.121   | 5.8                                 | 7.6–29.2                               | $9.5 \times 10^{-3}$ – $1.3 \times 10^{-1}$                    |
| HCl                           | 0.047   | 4.7                                 | 10.4–29.5                              | $8.2 \times 10^{-3}$ – $1.1 \times 10^{-1}$                    |
| NO <sub>3</sub> <sup>-</sup>  | 0.027   | 2.7                                 | 5.4–28.8                               | $2.2 \times 10^{-2}$ – $2.4 \times 10^{-1}$                    |
| NO <sub>2</sub> <sup>-</sup>  | 0.034   | 3.0                                 | 3.0–16.0                               | $6.1 \times 10^{-4}$ – $2.8 \times 10^{-2}$                    |
| SO <sub>4</sub> <sup>2-</sup> | 0.121   | 4.6                                 | 4.6–28.2                               | $1.2 \times 10^{-2}$ – $1.3 \times 10^{-1}$                    |
| Cl <sup>-</sup>               | 0.047   | 3.2                                 | 4.9–20.2                               | $6.6 \times 10^{-3}$ – $1.0 \times 10^{-1}$                    |

280

### 281 3.2 Concentrations of acidic species during the campaign

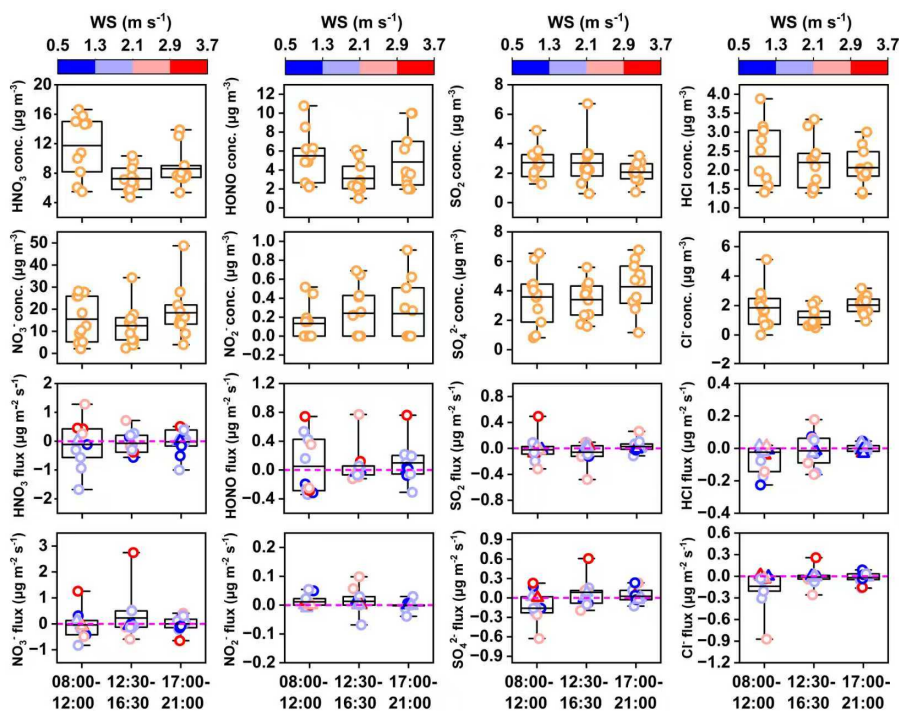
282 The diurnal variations of inorganic acidic gases (HNO<sub>3</sub>, HONO, SO<sub>2</sub>, HCl) and particulate ions  
 283 (NO<sub>3</sub><sup>-</sup>, NO<sub>2</sub><sup>-</sup>, SO<sub>4</sub><sup>2-</sup>, Cl<sup>-</sup>) in morning, afternoon and nighttime during the observation campaign are shown  
 284 in **Figure 2a**. At the sampling site, the mean concentration of total nitrogen-containing acidic species  
 285 (gaseous + particulate,  $8.4 \pm 8.0 \mu\text{g m}^{-3}$ ) was higher than that of sulfur-containing ( $3.1 \pm 1.5 \mu\text{g m}^{-3}$ ) and  
 286 chlorine-containing acidic species ( $2.0 \pm 0.8 \mu\text{g m}^{-3}$ ), indicating that atmospheric acidic species at the  
 287 site was dominated by nitrogen species.

288 Gaseous HNO<sub>3</sub> and HONO showed similar diurnal patterns of higher concentrations in morning and  
 289 nighttime than at noon. The diurnal pattern is mainly driven by the diurnal evolution of the atmospheric  
 290 boundary layer (Finlayson-Pitts and Pitts 1999, Lin et al. 2006). HONO has multiple sources including



291 combustion (Nie et al. 2015) and soil emissions (Su et al. 2011), as well as secondary formation from  
292 gas-phase  $\text{NO} + \text{OH}$  reaction and heterogeneous  $\text{NO}_2$  reaction on moist surfaces (Baergen and Donaldson  
293 2016, Liu et al. 2014, Villena et al. 2011, Wong et al. 2012). Its low noontime levels are mainly due to  
294 rapid daytime photolytic loss. In contrast,  $\text{SO}_2$  and  $\text{HCl}$  showed slightly higher daytime mean  
295 concentrations ( $\text{SO}_2$ :  $2.7 \pm 1.3 \mu\text{g m}^{-3}$ ;  $\text{HCl}$ :  $2.3 \pm 0.7 \mu\text{g m}^{-3}$ ) than nighttime ( $\text{SO}_2$ :  $2.1 \pm 0.7 \mu\text{g m}^{-3}$ ;  $\text{HCl}$ :  
296  $2.0 \pm 0.5 \mu\text{g m}^{-3}$ ), being likely related to daytime industrial emissions, as both species are mainly emitted  
297 from the combustion of sulfur- and chlorine-containing coal and wastes.

298 Particulate  $\text{NO}_3^-$ ,  $\text{SO}_4^{2-}$  and  $\text{Cl}^-$  showed higher concentrations in the morning ( $15.5 \pm 10.1$ ,  $3.6 \pm 1.9$ ,  
299  $1.8 \pm 1.4 \mu\text{g m}^{-3}$ ) and nighttime ( $18.4 \pm 11.9$ ,  $4.3 \pm 1.7$ ,  $2.0 \pm 0.6 \mu\text{g m}^{-3}$ ), and lower levels in afternoon  
300 ( $12.5 \pm 8.9$ ,  $3.4 \pm 1.2$ ,  $1.2 \pm 0.6 \mu\text{g m}^{-3}$ ). This pattern is mainly controlled by their formation pathways  
301 and diurnal boundary layer variation, consistent with previous studies (Chang et al. 2011, Trebs et al.  
302 2004, Young et al. 2022). Particulate  $\text{NO}_2^-$  had the lowest concentration ( $0.1\text{--}0.2 \mu\text{g m}^{-3}$ ) among the four  
303 ions, with lower concentrations in the morning ( $0.13 \pm 0.19 \mu\text{g m}^{-3}$ ) than afternoon ( $0.24 \pm 0.27 \mu\text{g m}^{-3}$ )  
304 and nighttime ( $0.24 \pm 0.32 \mu\text{g m}^{-3}$ ).



305

306

307

308

309

310

311

312

313

314

315

316

317

**Figure 2.** a. Box-and-whisker plots with data points of diurnal concentration variations of eight species (gaseous HNO<sub>3</sub>, HONO, SO<sub>2</sub>, HCl; particulate NO<sub>3</sub><sup>-</sup>, NO<sub>2</sub><sup>-</sup>, SO<sub>4</sub><sup>2-</sup>, Cl<sup>-</sup>) and b. Box-and-whisker plots overlaid with individual data points (coded by horizontal wind speed) showing REA-measured fluxes of eight inorganic species, grouped by diurnal time intervals. Horizontal lines mark means, and boxes denote interquartile ranges.

### 3.3 Observed flux of acidic species during the campaign

**Figure 2b** shows the diurnal variations and horizontal wind speed (WS) dependence of REA-measured fluxes for the eight acidic inorganic species, grouped by three diurnal time intervals. **Figure 3a** summarizes the flux detection rate (the proportion of flux events above the detection limit relative to the total number of measurements) and the mean ± standard deviation (SD) of flux values above the detection limits for each target species. The flux detection rates of the acidic species, ranked from highest to lowest, were 88% for HNO<sub>3</sub> and HONO, 82% for NO<sub>3</sub><sup>-</sup>, 79% for SO<sub>4</sub><sup>2-</sup>, 61% for SO<sub>2</sub> and Cl<sup>-</sup>, 48% for HCl, and



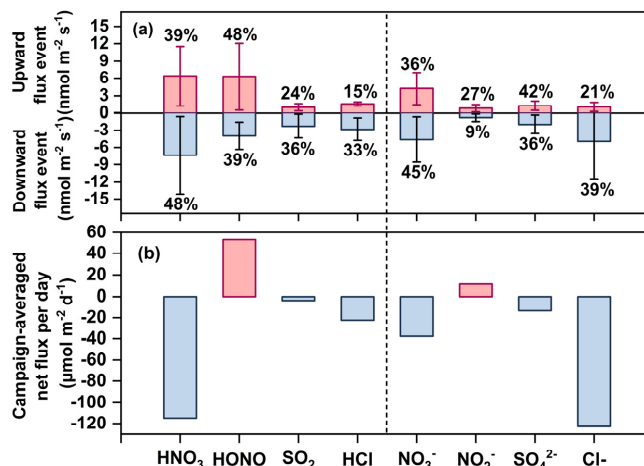
318 36% for  $\text{NO}_2^-$ . All investigated species showed bidirectional flux behavior, which were also observed in  
319 nearly all prior REA measurements from remote forest to urban grassland (**Figure 4**). If this is not an  
320 intrinsic artifact of the REA method, this demonstrates that surfaces across all atmospheric environments  
321 and land types in these studies are capable of emitting these inorganic acidic species into the atmosphere,  
322 rather than only serving as a deposition sink. The observed apparent fluxes presented here are modulated  
323 by deposition, emission, and probably chemical production/loss and the storage change below the 4-  
324 meter measurement height, therefore cannot be simply regarded as emission flux from the cropland or  
325 directly used to derive dry deposition velocity.  $\text{HNO}_3$  recorded the highest count of downward flux events  
326 (48% of the measurements) and the largest downward flux values ( $-7.5 \pm 6.7 \text{ nmol m}^{-2} \text{ s}^{-1}$ ) across all  
327 species, whereas  $\text{NO}_2^-$  had the lowest count (9%) and smallest values of downward flux ( $-0.87 \pm 0.65$   
328  $\text{nmol m}^{-2} \text{ s}^{-1}$ ). The downward fluxes of HONO ( $-0.19 \pm 0.11 \text{ } \mu\text{g m}^{-2} \text{ s}^{-1}$ ) and  $\text{NO}_3^-$  ( $-0.29 \pm 0.24 \text{ } \mu\text{g m}^{-2} \text{ s}^{-1}$ )  
329 at our site were 1-2 orders of magnitude higher than all prior measurements at rural/remote forest or  
330 grassland sites, while the negative fluxes of  $\text{HNO}_3$ ,  $\text{SO}_2$ ,  $\text{SO}_4^{2-}$  are comparable with prior reports (**Figure**  
331 **4**). This points to substantial nitrogen deposition (specifically, HONO and  $\text{NO}_3^-$ ) at this site, driven by  
332 industrial emissions in the surrounding area.

333 We focus specifically on the upward fluxes showing emissions of atmospheric acidic species from this  
334 cropland under the long-term influence of chemical industrial emissions. Key findings are summarized  
335 below: 1.  $\text{HNO}_3$  and HONO recorded far more upward flux events (39% and 48%) and upward flux  
336 values ( $6.4 \pm 5.2$  and  $6.3 \pm 5.7 \text{ nmol m}^{-2} \text{ s}^{-1}$ ) than  $\text{SO}_2$  and HCl, indicating significant production of both  
337 species below the measurement height. Furthermore, their counts of upward flux events and flux values  
338 were higher in the morning than in the afternoon and night (**Figure 2b**). This pattern points to strong  
339 nocturnal production pathways for both species:  $\text{HNO}_3$  and HONO accumulate in the surface layer



340 overnight under weak turbulent mixing, and result in pronounced upward fluxes in the next morning as  
 341 turbulence intensifies. 2. In terms of particulate species,  $\text{NO}_3^-$  had more upward flux events (36%) and  
 342 higher upward flux values ( $4.2 \pm 2.8 \text{ nmol m}^{-2} \text{ s}^{-1}$ ) than other three species. The most likely  $\text{NO}_3^-$  sources  
 343 are in-situ formation of ammonium nitrate near the surface layer from ammonia emitted by the cropland  
 344 or wind-blown particles from agricultural soils. 3. Like downward flux, HONO ( $0.30 \pm 0.27 \text{ } \mu\text{g m}^{-2} \text{ s}^{-1}$ )  
 345 and  $\text{NO}_3^-$  ( $0.26 \pm 0.17 \text{ } \mu\text{g m}^{-2} \text{ s}^{-1}$ ) again show one or two orders of magnitude higher upward fluxes at our  
 346 site than all prior measurements, while those of  $\text{HNO}_3$ ,  $\text{SO}_2$ ,  $\text{SO}_4^{2-}$  are comparable with prior reports  
 347 (Figure 4).

348 On the windy day of 24 December (highest mean horizontal wind speed  $3.8 \text{ m s}^{-1}$  in the campaign),  
 349 exceptionally high upward fluxes of  $\text{HNO}_3$ , HONO,  $\text{NO}_3^-$ , and  $\text{SO}_4^{2-}$  were recorded, exceeding those  
 350 from all other measurement days by one order of magnitude. After excluding this outlier, net fluxes over  
 351 the entire observation period were upward for HONO and  $\text{NO}_2^-$  (mean daily  $53.0$  and  $11.5 \text{ } \mu\text{mol m}^{-2} \text{ d}^{-1}$ ,  
 352 respectively), and negative for all other species:  $\text{HNO}_3$  ( $-114.9 \text{ } \mu\text{mol m}^{-2} \text{ d}^{-1}$ ),  $\text{Cl}^-$  ( $-122.9 \text{ } \mu\text{mol m}^{-2} \text{ d}^{-1}$ ),  
 353  $\text{NO}_3^-$  ( $-37.7 \text{ } \mu\text{mol m}^{-2} \text{ d}^{-1}$ ),  $\text{SO}_4^{2-}$  ( $-13.4 \text{ } \mu\text{mol m}^{-2} \text{ d}^{-1}$ ),  $\text{SO}_2$  ( $-3.7 \text{ } \mu\text{mol m}^{-2} \text{ d}^{-1}$ ), and  $\text{HCl}$  ( $-22.4 \text{ } \mu\text{mol m}^{-2}$   
 354  $\text{d}^{-1}$ ) (Figure 3b).



355



356 **Figure 3.** Flux detection rates (fraction of measurements above the detection limit) and mean  $\pm$  standard  
 357 deviation of flux values for the eight target species.

358

359 Analysis of wind speed (WS), ambient temperature (Ta), relative humidity (RH), and ultraviolet-

360 A radiation (UV-A) meteorological parameters (**Figure S4**) identified wind speed as a key regulator of

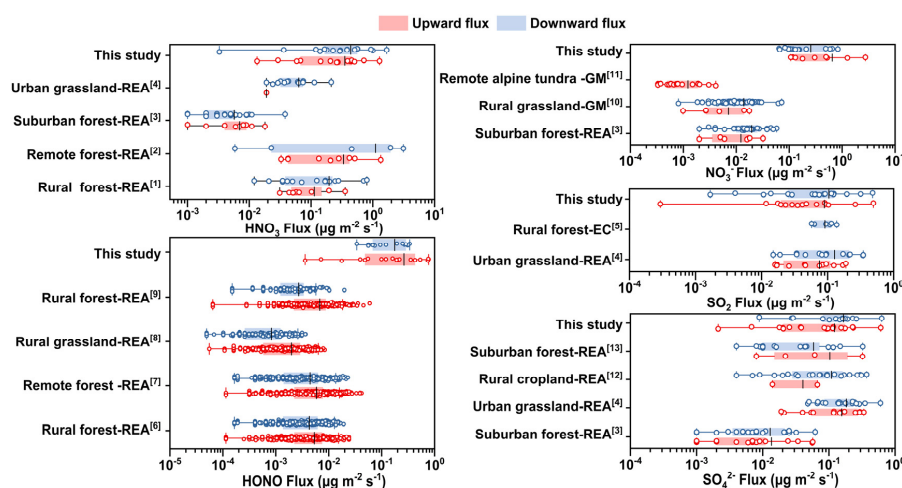
361 flux magnitude. Under low wind speeds, all target species exhibited predominantly downward or weak

362 upward fluxes (**Figure 2b**), while pronounced upward fluxes occurred almost exclusively at wind speeds  $>$

363  $2.1 \text{ m s}^{-1}$ . Notably, apparent deposition velocity ( $-F/C$ ) was correlated with friction velocity ( $u^*$ ) for both

364 upward and downward fluxes (**Figure 5**), demonstrating that turbulence intensity directly drives flux

365 magnitude.



366

367 Figure 4. The comparison of the fluxes observed in this study and those reported in the literature. We

368 primarily compiled REA-measured fluxes from the literature, supplementing with EC and GM

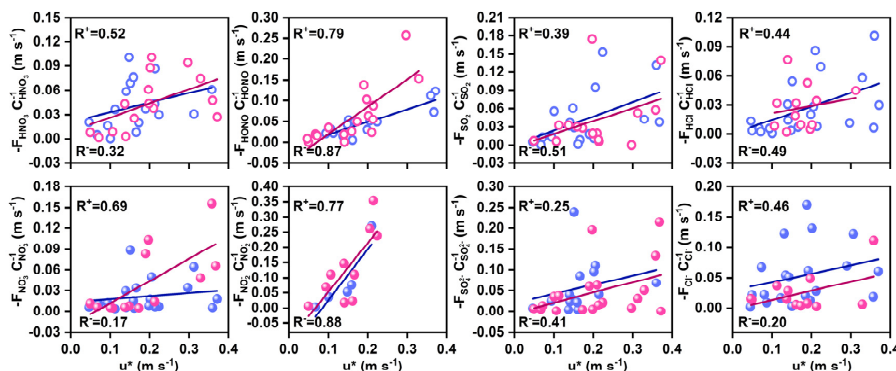
369 measurements due to the limited availability of REA flux data for  $\text{NO}_3^-$  and  $\text{SO}_2$ . [1] (Pryor et al. 2002),

370 [2] (Hansen et al. 2015), [3] (Xu et al. 2021), [4] (Myles et al. 2007), [5] (Meyers et al. 1998), [6]

371 (Zhou et al. 2011), [7] (Ren et al. 2011), [8] (von der Heyden et al. 2022), [9] (Zhang et al. 2012), [10]



372 (Huebert et al. 1988), [11] (Ratray and Sievering 2001), [12] (Meyers et al. 2006), [13] (Matsuda et al.  
373 2015).



374

375 **Figure 5.** Apparent deposition velocities (calculated as  $-F/C$  for downward fluxes and  $F/C$  for upward

376 fluxes) of inorganic acidic gases and particles versus friction velocity ( $u^*$ ). Red and blue symbols

377 denote upward and downward fluxes, respectively.

### 378 3.4 Gross upward fluxes of HNO<sub>3</sub> and HONO

379 The land surface is a well-documented source of HONO, which could originate from direct soil

380 emission, heterogeneous NO<sub>2</sub> reactions on diverse wet surfaces (e.g., bare ground, building exteriors,

381 urban grime, aerosol particles), and the photolysis of nitric acid/nitrate on leaf surfaces (Zhou et al. 2011).

382 Upward HNO<sub>3</sub> emissions have been widely observed over forests and grasslands (Hansen et al. 2015,

383 Myles et al. 2007, Nemitz et al. 2009, Pryor et al. 2002, Xu et al. 2021). For example, Hansen et al. (2015)

384 reported that about 70% of the total samples showed HNO<sub>3</sub> emission during late summer/autumn in a

385 mixed deciduous forest site in the USA. Xu et al. (2021) showed about 30% of the total samples showed

386 apparent HNO<sub>3</sub> emissions at a suburban forest site in Japan. HNO<sub>3</sub> is thought to deposit with a zero

387 resistance even over slightly wet surfaces, where it can also be formed via  $NO_2 + H_2O_{(surface)} \rightarrow$

388  $HONO + HNO_3$  and  $NO_2 + H_2O_{(surface)} \rightarrow HONO + HNO_3$ . Potential upward HNO<sub>3</sub> fluxes

389 probably arise from decomposition of NH<sub>4</sub>NO<sub>3</sub> aerosols near warm surfaces and deposited NH<sub>4</sub>NO<sub>3</sub> on



390 the ground or leaf surfaces as water layers evaporate.

391 The gross upward flux ( $F_{gross}$ ) can be calculated from the apparent flux observed at the  
392 measurement height ( $F$ ) and the surface deposition ( $D$ ) via  $F_{gross} = F + D$  (Schobesberger et al. 2016).  
393 Unlike the apparent flux that is confounded by concurrent atmospheric deposition,  $F_{gross}$  reflects more  
394 accurately the actual emission from the near-surface layer to the atmosphere. In this study, we estimated  
395  $F_{gross}$  for  $\text{HNO}_3$  and HONO, owing to not only the pronounced positive apparent fluxes of these two  
396 species (**Figure 3**) but also the feasibility of approximating their dry deposition velocities given their  
397 relatively high water solubility.

398 According to Wesely (2007) resistance model, physical deposition velocity of a molecule from the  
399 atmosphere to the surface is calculated as  $V_d = \frac{1}{R_a + R_b + R_c}$ , where  $R_a$ ,  $R_b$ , and  $R_c$  are aerodynamic  
400 resistance, molecular diffusion resistance and surface resistance, respectively. For highly water-soluble  
401  $\text{HNO}_3$ ,  $R_c$  is near zero; for water-soluble HONO,  $R_c$  over slight wet surfaces (like vegetable surface in  
402 the cropland) is also far smaller than  $R_a$  (Harrison et al. 1996). Thus,  $V_d$  for both species can be simplified  
403 to  $V_d \approx \frac{1}{R_a + R_b}$ . Substituting the standard formulations  $R_a = \frac{\ln(\frac{z}{z_0}) - \psi_m}{k \cdot u_*}$  and  $R_b = \frac{2 \cdot S_c^{\frac{2}{3}}}{k \cdot u_*}$  into the  
404 simplified  $V_d$  equation yields

$$405 \quad V_d \approx \frac{k \cdot u_*}{\ln(\frac{z}{z_0}) - \psi_m + 2 \cdot S_c^{\frac{2}{3}}} \quad (3)$$

406 where  $k$  is the von Karman constant,  $u_*$  is friction velocity,  $z$  is measurement height,  $z_0$  is roughness  
407 length, which is constant at a winter underlying surface,  $\psi_m$  is the Businger dimensionless momentum  
408 stability function, and  $S_c$  is the Schmidt number. Our sampling conditions (4 m measurement height,  
409 cloudy winter days, 5–20°C temperature range) resulted in only 3–4% diurnal variation in  $S_c$  and ~1.0–  
410 1.1 variation in  $\psi_m$ . The corresponding 10%–14% relative variation in the denominator of Equation (3)  
411 justifies a linear approximation  $V_d = a \cdot u_*$ , where  $a$  is an empirical constant. Substituting surface deposition



412  $D = V_d \cdot C$  into the  $F_{gross}$  definition gives

413 
$$F_{gross} = F + a \cdot u^* \cdot C \quad (4)$$

414 From Equation (4),  $a - \frac{F_{gross}/C}{u^*}$  is equal to  $\frac{-F/C}{u^*}$ , which is the slopes of the data points in **Figure 5**. We

415 calculated the empirical constant  $a$ , for  $\text{HNO}_3$  and HONO separately, from the maximum slope

416  $\left(\frac{-F/C}{u^*}\right)_{max}$  of the downward-flux data points in **Figure 5**, when  $F_{gross}=0$  (that is, no upward emission

417 and apparent flux equals deposition).  $a$  was then substituted into Equation (4) to calculate  $F_{gross}$  for all

418 the sampling periods. Please note that according to the mass balance equation ( $S = P - L + E - D - F$ ),

419  $F_{gross}$  includes joint contributions from surface emission ( $E$ ), net chemical production below the

420 measurement height ( $P-L$ ) and the storage change flux below the measurement height ( $S$ ,  $\int_0^h \frac{\delta S_X(Z)}{\delta t} \delta Z$ ),

421 which are not distinguishable in our estimation of  $F_{gross}$

422 
$$F_{gross} = P + E - S \quad (5)$$

423 Based on the calculation from Equation (4), the diurnal variations in upward gross fluxes of  $\text{HNO}_3$

424 and HONO, along with their dependence on horizontal wind speed or ambient temperature, are presented

425 in **Figure 6**. Overall,  $\text{HNO}_3$  gross fluxes ( $1.1 \pm 0.9 \mu\text{g m}^{-2} \text{s}^{-1}$ ) were higher than those of HONO ( $0.4 \pm 0.4$

426  $\mu\text{g m}^{-2} \text{s}^{-1}$ ).  $\text{HNO}_3$  gross fluxes were higher in the morning ( $1.6 \pm 1.4 \mu\text{g m}^{-2} \text{s}^{-1}$ ) than in the afternoon

427 ( $0.9 \pm 0.4 \mu\text{g m}^{-2} \text{s}^{-1}$ ) and nighttime ( $0.7 \pm 0.5 \mu\text{g m}^{-2} \text{s}^{-1}$ ). Fluxes under high wind speeds ( $WS > 2.1 \text{ m s}^{-1}$ ,

428  $1.8 \pm 1.1 \mu\text{g m}^{-2} \text{s}^{-1}$ ) were significantly greater than those under low wind speeds ( $0.6 \pm 0.4 \mu\text{g m}^{-2} \text{s}^{-1}$ ),

429 indicating that upward gross fluxes of  $\text{HNO}_3$  below the measurement height were accelerated under

430 elevated wind speed.

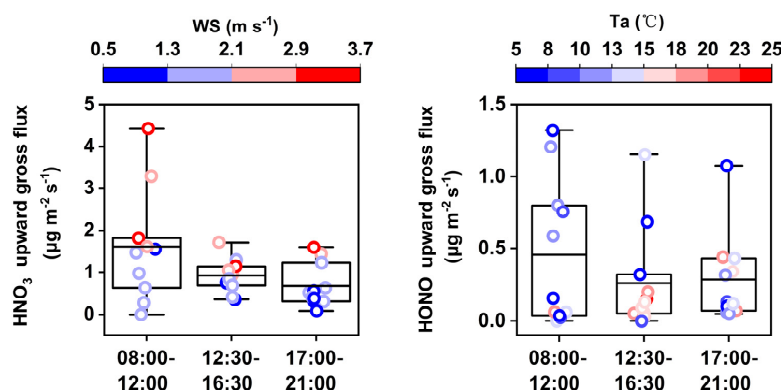
431 Similar to  $\text{HNO}_3$ , HONO gross fluxes were higher in the morning ( $0.5 \pm 0.5 \mu\text{g m}^{-2} \text{s}^{-1}$ ) than in the

432 afternoon ( $0.3 \pm 0.3 \mu\text{g m}^{-2} \text{s}^{-1}$ ) and nighttime ( $0.3 \pm 0.3 \mu\text{g m}^{-2} \text{s}^{-1}$ ). In contrast to  $\text{HNO}_3$ , HONO emission

433 fluxes showed no significant correlation with wind speed, solar radiation, or relative humidity (**Figure**



434 S5); instead, the fluxes were significantly higher under low temperatures ( $T_a < 15^\circ\text{C}$ ,  $0.4 \pm 0.5 \mu\text{g m}^{-2} \text{s}^{-1}$ )  
 435  $^1$ ) than under high temperatures ( $0.1 \pm 0.1 \mu\text{g m}^{-2} \text{s}^{-1}$ ). This behavior is likely attributed to the dependence  
 436 of HONO surface production from aqueous-phase reactions in soil pore water or surface water films (Ren  
 437 et al. 2020, Wu et al. 2019). High temperatures reduce soil and surface moisture, thereby suppressing  
 438 HONO production.



439  
 440 **Figure 6.** Box-and-whisker plots overlaid with individual data points (coded by horizontal wind speed  
 441 and ambient temperature) showing upward gross fluxes of HNO<sub>3</sub> and HONO, grouped by diurnal time  
 442 intervals. Horizontal lines mark medians, and boxes denote interquartile ranges.

#### 443 4. Conclusions

444 In this study, we developed a Relaxed Eddy Accumulation system capable of simultaneous flux  
 445 measurement of eight gaseous and particulate inorganic acidic species, targeting urban cropland under  
 446 long-term exposure to chemical industry emissions. The system achieved a relative uncertainty of air  
 447 sample volume < 0.2%, a lag time-induced analyte mass uncertainty of 2.64%, and a relative uncertainty  
 448 of mass analysis ranging from 2.7% to 5.8%. Using Gaussian error propagation and the t-test method,  
 449 we determined that the flux measurement precision of the system ranges from 3.0% to 29.5%, and the  
 450 flux detection limits span from  $6.1 \times 10^{-4}$  to  $2.4 \times 10^{-1} \mu\text{g m}^{-2} \text{s}^{-1}$ , depending on the chemical species,



451 ambient atmospheric concentrations and flux magnitudes during the sampling periods.

452       The flux detection rates ranged from 36% ( $\text{NO}_2^-$ ) to 88% ( $\text{HNO}_3$  and HONO) during the winter  
453 observation period. All inorganic acid species exhibited bidirectional flux behavior, demonstrating that  
454 cropland can act as a source of inorganic acidic species to the atmosphere, rather than only serving as a  
455 deposition sink.  $\text{HNO}_3$ ,  $\text{NO}_3^-$  and HONO were the dominant contributors to upward fluxes, with far more  
456 frequent emission events and larger flux values than other species. The diurnal pattern points to strong  
457 nocturnal production in the surface layer overnight under weak turbulent mixing, and pronounced upward  
458 fluxes in the next morning as turbulence intensifies. The apparent deposition velocities of all species  
459 were positively correlated with friction velocity for both upward and downward fluxes, highlighting the  
460 key regulatory role of turbulent mixing in acidic species exchange. Over the winter observation period  
461 (excluding one high-wind outlier day), HONO and  $\text{NO}_2^-$  showed net emission fluxes, while all other  
462 species exhibited net deposition.

463       Based on the mass balance equation and resistance in-series model, we estimated the gross upward  
464 fluxes of water-soluble  $\text{HNO}_3$  and HONO. The gross flux of  $\text{HNO}_3$  was accelerated under elevated  
465 turbulence, while HONO gross flux was enhanced at lower ambient temperatures, likely due to elevated  
466 soil and surface moisture. Our results provide critical observational data and mechanistic insights into  
467 acidic species exchange over cropland under the long-term influence of chemical industrial emissions in  
468 an urban environment.

469

470 **Data availability.** The data used in this article will be uploaded to public data repository, once the article  
471 is accepted.

#### 472 **Acknowledgments**

473 This research was supported by the National Key Research and Development Program of China (grant



474 no. 2023YFC3709801), the National Natural Science Foundation of China (grant no. 42175131), and the  
475 Fundamental Research Funds (grant no. G1323523063) for the Central Universities, China University of  
476 Geosciences (Wuhan).

477 **Competing interests**

478 The contact author has declared that none of the authors has any competing interests.

479 **Author contributions.**

480 HY designed the study. HY, XW, and JS built the REA system. JH, XW, and HY characterized the system.  
481 JH, XW, YW, ZL, ZH, and QW contributed to field measurement. JH and HY analyzed the data and  
482 wrote the manuscript.

483 **Reference:**

- 484 Aber, J., McDowell, W., Nadelhoffer, K., Magill, A., Berntson, G., Kamakea, M., McNulty, S., Currie,  
485 W., Rustad, L. and Fernandez, I. (1998) Nitrogen Saturation in Temperate Forest Ecosystems.  
486 *BioScience* 48(11), 921-934.
- 487 Baergen, A.M. and Donaldson, D.J. (2016) Formation of reactive nitrogen oxides from urban grime  
488 photochemistry. *Atmospheric Chemistry and Physics* 16(10), 6355-6363.
- 489 Businger, J.A. and Oncley, S.P. (1990) Flux Measurement with Conditional Sampling. *Journal of*  
490 *Atmospheric and Oceanic Technology* 7(2), 349-352.
- 491 Chang, L.T.-C., Tsai, J.-H., Lin, J.-M., Huang, Y.-S. and Chiang, H.-L. (2011) Particulate matter and  
492 gaseous pollutants during a tropical storm and air pollution episode in Southern Taiwan.  
493 *Atmospheric Research* 99(1), 67-79.
- 494 Farmer, D.K., Chen, Q., Kimmel, J.R., Docherty, K.S., Nemitz, E., Artaxo, P.A., Cappa, C.D., Martin,  
495 S.T. and Jimenez, J.L. (2013) Chemically Resolved Particle Fluxes Over Tropical and Temperate



- 496 Forests. *Aerosol Science & Technology* 47(7), 818-830.
- 497 Farmer, D.K., Kimmel, J.R., Phillips, G., Docherty, K.S., Worsnop, D.R., Sueper, D., Nemitz, E. and  
498 Jimenez, J.L. (2011) Eddy covariance measurements with high-resolution time-of-flight aerosol  
499 mass spectrometry: a new approach to chemically resolved aerosol fluxes. *Atmospheric*  
500 *Measurement Techniques* 4(6), 1275-1289.
- 501 Finlayson-Pitts, B.J. and Pitts, J.J.N. (1999) *Chemistry of the Upper and Lower Atmosphere: Theory,*  
502 *Experiments and Applications, Chemistry of the Upper and Lower Atmosphere: Theory,*  
503 *Experiments and Applications.*
- 504 Fitz, D.R. and Millar, B. (2002) Evaluation of diffusion denuder coatings for removing acid gases from  
505 ambient air, US Environmental Protection Agency, Office of Air Quality Planning and Standards,  
506 Emissions, Monitoring, and Analysis Division.
- 507 Galloway, J.N. (1995) Acid deposition: Perspectives in time and space. *Water, Air, and Soil Pollution*  
508 85(1), 15-24.
- 509 Gaman, A., Rannik, Ü., Aalto, P., Pohja, T., Siivola, E., Kulmala, M. and Vesala, T. (2004) Relaxed Eddy  
510 Accumulation System for Size-Resolved Aerosol Particle Flux Measurements. *Journal of*  
511 *Atmospheric and Oceanic Technology* 21(6), 933-943.
- 512 Gordon, M., Staebler, R.M., Liggio, J., Vlasenko, A., Li, S.M. and Hayden, K. (2011) Aerosol flux  
513 measurements above a mixed forest at Borden, Ontario. *Atmospheric Chemistry and Physics* 11(14).
- 514 Hansen, K., Pryor, S.C., Boegh, E., Hornsby, K.E., Jensen, B. and Sørensen, L.L. (2015) Background  
515 concentrations and fluxes of atmospheric ammonia over a deciduous forest. *Agricultural and Forest*  
516 *Meteorology* 214-215, 380-392.
- 517 Harrison, R.M., Peak, J.D. and Collins, G.M. (1996) Tropospheric cycle of nitrous acid. *Journal of*



- 518 Geophysical Research: Atmospheres 101(D9), 14429-14439.
- 519 Huebert, B.J., Luke, W.T., Delany, A.C. and Brost, R.A. (1988) Measurements of concentrations and dry  
520 surface fluxes of atmospheric nitrates in the presence of ammonia. Journal of Geophysical Research  
521 Atmospheres 93(D6).
- 522 Huebert, B.J. and Robert, C.H. (1985) The dry deposition of nitric acid to grass. Journal of Geophysical  
523 Research: Atmospheres 90(D1), 2085-2090.
- 524 Karl, T., Harley, P., Guenther, A., Rasmussen, R., Baker, B., Jardine, K. and Nemitz, E. (2005) The bi-  
525 directional exchange of oxygenated VOCs between a loblolly pine (*Pinus taeda*) plantation and the  
526 atmosphere. Atmospheric Chemistry and Physics 5(11), 3015-3031.
- 527 Kljun, N., Calanca, P., Rotach, M.W. and Schmid, H.P. (2015) A simple two-dimensional  
528 parameterisation for Flux Footprint Prediction (FFP). Geoscientific Model Development 8(11),  
529 3695-3713.
- 530 Laufs, S., Cazaunau, M., Stella, P., Kurtenbach, R., Cellier, P., Mellouki, A., Loubet, B. and Kleffmann,  
531 J. (2017) Diurnal fluxes of HONO above a crop rotation. Atmospheric Chemistry and Physics  
532 17(11), 6907-6923.
- 533 Lee, A., Schade, G.W., Holzinger, R. and Goldstein, A.H. (2005) A comparison of new measurements of  
534 total monoterpene flux with improved measurements of speciated monoterpene flux. Atmospheric  
535 Chemistry and Physics 5(2), 505-513.
- 536 Lin, Y.-C., Cheng, M.-T., Ting, W.-Y. and Yeh, C.-R. (2006) Characteristics of gaseous HNO<sub>2</sub>, HNO<sub>3</sub>,  
537 NH<sub>3</sub> and particulate ammonium nitrate in an urban city of Central Taiwan. Atmospheric  
538 Environment 40(25), 4725-4733.
- 539 Liu, Z., Wang, Y., Costabile, F., Amoroso, A., Zhao, C., Huey, L.G., Stickel, R., Liao, J. and Zhu, T.



- 540 (2014) Evidence of Aerosols as a Media for Rapid Daytime HONO Production over China.  
541 Environmental Science & Technology 48(24), 14386-14391.
- 542 Matsuda, K., Watanabe, I., Mizukami, K., Ban, S. and Takahashi, A. (2015) Dry deposition of PM2.5  
543 sulfate above a hilly forest using relaxed eddy accumulation. Atmospheric Environment 107, 255-  
544 261.
- 545 Meng, F., Qin, M., Fang, W., Duan, J., Tang, K., Zhang, H., Shao, D., Liao, Z., Feng, Y., Huang, Y., Ni,  
546 T., Xie, P., Liu, J. and Liu, W. (2022) Measurement of HONO flux using the aerodynamic gradient  
547 method over an agricultural field in the Huaihe River Basin, China. Journal of Environmental  
548 Sciences 114, 297-307.
- 549 Meyers, T.P., Finkelstein, P., Clarke, J., Ellestad, T.G. and Sims, P.F. (1998) A multilayer model for  
550 inferring dry deposition using standard meteorological measurements. Journal of Geophysical  
551 Research: Atmospheres 103(D17), 22645-22661.
- 552 Meyers, T.P., Huebert, B.J. and Hicks, B.B. (1989) HNO<sub>3</sub> deposition to a deciduous forest. Boundary-  
553 Layer Meteorology 49(4), 395-410.
- 554 Meyers, T.P., Luke, W.T. and Meisinger, J.J. (2006) Fluxes of ammonia and sulfate over maize using  
555 relaxed eddy accumulation. Agricultural and Forest Meteorology 136(3-4), 203-213.
- 556 Myles, L., Meyers, T.P. and Robinson, L. (2007) Relaxed eddy accumulation measurements of ammonia,  
557 nitric acid, sulfur dioxide and particulate sulfate dry deposition near Tampa, FL, USA.  
558 ENVIRONMENTAL RESEARCH LETTERS 2(3), 034004.
- 559 Nemitz, E., Dorsey, J.R., Flynn, M.J., Gallagher, M.W., Hensen, A., Erisman, J.W., Owen, S.M.,  
560 Dämmgen, U. and Sutton, M.A. (2009) Aerosol fluxes and particle growth above managed grassland.  
561 Biogeosciences 6(8), 1627-1645.



- 562 Nemitz, E., Sutton, M.A., Wyers, G.P., Otjes, R.P., Mennen, M.G., van Putten, E.M. and Gallagher, M.W.  
563 (2004) Gas-particle interactions above a Dutch heathland: II. Concentrations and surface exchange  
564 fluxes of atmospheric particles. *Atmospheric Chemistry and Physics* 4(4), 1007-1024.
- 565 Nguyen, T.B., Crouse, J.D., Teng, A.P., St Clair, J.M., Paulot, F., Wolfe, G.M. and Wennberg, P.O. (2015)  
566 Rapid deposition of oxidized biogenic compounds to a temperate forest. *Proceedings of the National  
567 Academy of Sciences of the United States of America* 112(5), E392-E401.
- 568 Nie, W., Ding, A.J., Xie, Y.N., Xu, Z., Mao, H., Kerminen, V.M., Zheng, L.F., Qi, X.M., Huang, X., Yang,  
569 X.Q., Sun, J.N., Herrmann, E., Petäjä, T., Kulmala, M. and Fu, C.B. (2015) Influence of biomass  
570 burning plumes on HONO chemistry in eastern China. *Atmospheric Chemistry and Physics* 15(3),  
571 1147-1159.
- 572 Poor, N., Pribble, R. and Greening, H. (2001) Direct wet and dry deposition of ammonia, nitric acid,  
573 ammonium and nitrate to the Tampa Bay Estuary, FL, USA. *Atmospheric Environment* 35(23),  
574 3947-3955.
- 575 Pryor, S.C., Barthelmie, R.J., Jensen, B., Jensen, N.O. and Sørensen, L.L. (2002) HNO<sub>3</sub> fluxes to a  
576 deciduous forest derived using gradient and REA methods. *Atmospheric Environment* 36(39), 5993-  
577 5999.
- 578 Pryor, S.C., Barthelmie, R.J., Sørensen, L.L. and Jensen, B. (2001) Ammonia concentrations and fluxes  
579 over a forest in the midwestern USA. *Atmospheric Environment* 35(32), 5645-5656.
- 580 Pryor, S.C., Larsen, S.E., Sørensen, L.L., Barthelmie, R.J., Grönholm, T., Kulmala, M., Launiainen, S.,  
581 Rannik, Ü. and Vesala, T. (2007) Particle fluxes over forests: Analyses of flux methods and  
582 functional dependencies. *Journal of Geophysical Research: Atmospheres* 112(D7).
- 583 Rattray, G. and Sievering, H. (2001) Dry deposition of ammonia, nitric acid, ammonium, and nitrate to



- 584 alpine tundra at Niwot Ridge, Colorado. *Atmospheric Environment* 35(6), 1105-1109.
- 585 Ren, X., Sanders, J.E., Rajendran, A., Weber, R.J., Goldstein, A.H., Pusede, S.E., Browne, E.C., Min,  
586 K.E. and Cohen, R.C. (2011) A relaxed eddy accumulation system for measuring vertical fluxes of  
587 nitrous acid. *Atmospheric Measurement Techniques* 4(10), 2093-2103.
- 588 Ren, Y., Stieger, B., Spindler, G., Grosselin, B., Mellouki, A., Tuch, T., Wiedensohler, A. and Herrmann,  
589 H. (2020) Role of the dew water on the ground surface in HONO distribution: a case measurement  
590 in Melpitz. *Atmospheric Chemistry and Physics* 20(21), 13069-13089.
- 591 Rumsey, I.C. and Walker, J.T. (2016) Application of an online ion-chromatography-based instrument for  
592 gradient flux measurements of speciated nitrogen and sulfur. *Atmospheric Measurement Techniques*  
593 9(6), 2581-2592.
- 594 Scharko, N.K., Schütte, U.M.E., Berke, A.E., Banina, L., Peel, H.R., Donaldson, M.A., Hemmerich, C.,  
595 White, J.R. and Raff, J.D. (2015) Combined Flux Chamber and Genomics Approach Links Nitrous  
596 Acid Emissions to Ammonia Oxidizing Bacteria and Archaea in Urban and Agricultural Soil.  
597 *Environmental Science & Technology* 49(23), 13825-13834.
- 598 Schobesberger, S., Lopez-Hilfiker, F.D., Taipale, D., Millet, D.B., D'Ambro, E.L., Rantala, P.,  
599 Mammarella, I., Zhou, P., Wolfe, G.M., Lee, B.H., Boy, M. and Thornton, J.A. (2016) High upward  
600 fluxes of formic acid from a boreal forest canopy. *Geophysical Research Letters* 43(17), 9342-9351.
- 601 Shaw, W.J., Spicer, C.W. and Kenny, D.V. (1998) Eddy correlation fluxes of trace gases using a tandem  
602 mass spectrometer. *Atmospheric Environment* 32(17), 2887-2898.
- 603 Shen, Jianlin, Chen, Deli, Bai, Mei, Sun, Jianlei, Lam and Shu (2018) Spatial variations in soil and plant  
604 nitrogen levels caused by ammonia deposition near a cattle feedlot. *Atmospheric Environment*.
- 605 Skov, H., Brooks, S. B., Goodsite, M. E., Lindberg, Steve E., Meyers, T. P., Landis, M. S., Larsen, M.,



- 606 Jensen, B., McConville, G., Christensen, J. (2006) Fluxes of reactive gaseous mercury measured  
607 with a newly developed method using relaxed eddy accumulation. *Atmospheric Environment*  
608 40(28), 5452-5463
- 609 Sievering, H., Kelly, T., McConville, G., Seibold, C. and Turnipseed, A. (2001) Nitric acid dry deposition  
610 to conifer forests:: Niwot Ridge spruce–fir–pine study. *Atmospheric Environment* 35(22), 3851-  
611 3859.
- 612 Su, H., Cheng, Y., Oswald, R., Behrendt, T., Trebs, I., Meixner, F.X., Andreae, M.O., Cheng, P., Zhang,  
613 Y. and Pöschl, U. (2011) Soil Nitrite as a Source of Atmospheric HONO and OH Radicals. *Science*  
614 333(6049), 1616-1618.
- 615 Trebs, I., Meixner, F.X., Slanina, J., Otjes, R., Jongejan, P. and Andreae, M.O. (2004) Real-time  
616 measurements of ammonia, acidic trace gases and water-soluble inorganic aerosol species at a rural  
617 site in the Amazon Basin. *Atmospheric Chemistry and Physics* 4(4), 967-987.
- 618 van Breemen, N. and van Dijk, H.F.G. (1988) Ecosystem effects of atmospheric deposition of nitrogen  
619 in The Netherlands. *Environmental Pollution* 54(3), 249-274.
- 620 Villena, G., Kleffmann, J., Kurtenbach, R., Wiesen, P., Lissi, E., Rubio, M.A., Croxatto, G. and  
621 Rappenglück, B. (2011) Vertical gradients of HONO, NO<sub>x</sub> and O<sub>3</sub> in Santiago de Chile.  
622 *Atmospheric Environment* 45(23), 3867-3873.
- 623 Vitousek, P.M. and Howarth, R.W. (1991) Nitrogen limitation on land and in the sea: How can it occur?  
624 *Biogeochemistry* 13(2), 87-115.
- 625 von der Heyden, L., Wißdorf, W., Kurtenbach, R. and Kleffmann, J. (2022) A relaxed eddy accumulation  
626 (REA) LOPAP system for flux measurements of nitrous acid (HONO). *Atmospheric Measurement*  
627 *Techniques* 15(6), 1983-2000.



- 628 Wesely, M.L. (2007) Parameterization of surface resistances to gaseous dry deposition in regional-scale  
629 numerical models. *Atmospheric Environment* 41, 52-63.
- 630 Wong, K.W., Tsai, C., Lefer, B., Haman, C., Grossberg, N., Brune, W.H., Ren, X., Luke, W. and Stutz, J.  
631 (2012) Daytime HONO vertical gradients during SHARP 2009 in Houston, TX. *Atmospheric*  
632 *Chemistry and Physics* 12(2), 635-652.
- 633 Wu, D., Horn, M.A., Behrendt, T., Müller, S., Li, J., Cole, J.A., Xie, B., Ju, X., Li, G., Ermel, M., Oswald,  
634 R., Fröhlich-Nowoisky, J., Hoor, P., Hu, C., Liu, M., Andreae, M.O., Pöschl, U., Cheng, Y., Su, H.,  
635 Trebs, I., Weber, B. and Sörgel, M. (2019) Soil HONO emissions at high moisture content are driven  
636 by microbial nitrate reduction to nitrite: tackling the HONO puzzle. *The ISME Journal* 13(7), 1688-  
637 1699.
- 638 Xu, M., Kasahara, K., Sorimachi, A. and Matsuda, K. (2021) Nitric acid dry deposition associated with  
639 equilibrium shift of ammonium nitrate above a forest by long-term measurement using relaxed eddy  
640 accumulation. *Atmospheric Environment* 256, 118454.
- 641 Young, L.-H., Hsiao, T.-C., Griffith, S.M., Huang, Y.-H., Hsieh, H.-G., Lin, T.-H., Tsay, S.-C., Lin, Y.-J.,  
642 Lai, K.-L., Lin, N.-H. and Lin, W.-Y. (2022) Secondary inorganic aerosol chemistry and its impact  
643 on atmospheric visibility over an ammonia-rich urban area in Central Taiwan. *Environmental*  
644 *Pollution* 312, 119951.
- 645 Zhang, N., Zhou, X., Bertman, S., Tang, D., Alaghmand, M., Shepson, P.B. and Carroll, M.A. (2012)  
646 Measurements of ambient HONO concentrations and vertical HONO flux above a northern  
647 Michigan forest canopy. *Atmospheric Chemistry and Physics* 12(17), 8285-8296.
- 648 Zhou, XL, Zhang, TerAvest, Tang and Hou (2011) Nitric acid photolysis on forest canopy surface as a  
649 source for tropospheric nitrous acid. *Nature Geoscience*.

<https://doi.org/10.5194/egusphere-2026-2234>

Preprint. Discussion started: 22 April 2026

© Author(s) 2026. CC BY 4.0 License.



650